Microwave Sensor Based on a Self-Modulated Oscillator

Mabel Pontón, *Member, IEEE*, Sergio Sancho, *Senior Member, IEEE*, and Almudena Suárez, *Fellow, IEEE*

***Abstract*—We propose a new type of oscillator sensor based on a self-modulated oscillator, exhibiting two concurrent oscillations at high and low frequency. To ensure a low phase noise, a high-frequency design is based on a stepped-impedance resonator, over which the material under test (MUT) is placed. The low-frequency oscillation is achieved through the introduction of feedback elements in the bias circuitry, by following a systematic procedure based on the use of stability circles and a rigorous two-stage stability analysis. The low-frequency oscillation modulates the high-frequency one and its harmonic components, generating multiple spectral lines around each of these components. For the first time to our knowledge, we demonstrate the simultaneous influence of the MUT on two concurrent oscillations, coupled through the nonlinear effects of the active device, as explained using an envelope-domain formulation. Thus, the sensing is based on the central frequency, frequency spacing, and amplitude of the spectral lines, enhancing both sensitivity and reliability. This multivariable approach enables robust multipoint detection and is expected to offer higher sensitivity compared with traditional methods that rely on a single oscillation frequency and amplitude. We present a calibration procedure, based on these measurands, to determine the real and imaginary parts of the MUT dielectric constant. The circuit has been fabricated and experimentally characterized, yielding very good results.**

***Index Terms*—Concurrent oscillations, envelope transient, sensor.**

I. Introduction

MICROWAVE sensors are highly sensitive to material properties, cost-effective, and easily integrated with planar fabrication processes [1], [2], [3], [4], [5]. In oscillator sensors [6], [7], [8], [9], [10], the passive structure, influenced by the material under test (MUT), is connected to an active core that enables autonomous operation. Variations in the MUT can be measured using frequency and amplitude detection interfaces [11], [12], [13], [14], [15], [16], allowing for a compact implementation. Due to their intrinsic gain, oscillator-based sensors can offer higher sensitivity compared with their passive equivalents. Most of these sensors function in a free-running mode [6], [7], [8], [9], [10], [11], [12], [13], [14], [15], [16], where the oscillation frequency changes in response to the MUT. Recent studies have also introduced sensors that use injection-locked oscillators [17], [18], [19], [20], [21], [22], [23]. In [17], [18], and [19], the sensing mechanism relies on detecting the phase shift between two oscillator circuits, both locked to the same input source, with only one oscillator being influenced by the sensing parameter. When using a single oscillator, sensing can be based on shifts in the central frequency of the locking band [20] or changes in both the central frequency and bandwidth [21], [22]. An alternative sensing mechanism [23], [24] relies on detecting variations in the beat frequency near the locking edges. The work [25] proposed a cascade of two high-frequency oscillators, at f_1 and f_2, with a frequency difference on the order of megahertz, such that only one (e.g., the oscillator at f_1) is affected by the MUT. Then, odd intermodulation products such as $2f_1 - f_2$ and $3f_1 - 2f_2$ enable multiplication of the frequency sensitivity by 2, 3, and so on. This implementation requires two distinct oscillators, for which mutual locking must be avoided. It may also suffer from high noise, as both the oscillations occur at high frequencies.

In [26], we presented a summary of newly developed analysis methods for both free-running and injection-locked sensors. Here we expand on [26] by proposing a new type of oscillator sensor, based on a self-modulated free-running oscillator. Two oscillations, at high and low frequency (f_{high} and f_{low}, respectively), are concurrently generated, so the circuit operates in a doubly autonomous quasi-periodic regime. Compared with [25], the two oscillation frequencies differ by several orders of magnitude and are simultaneously generated using a single active device, which enables low power consumption and compactness. Unlike [25], the two oscillations are influenced by the MUT due to the coupling inherent to the nonlinearity of the active device, which should enhance sensitivity.

The two concurrent frequencies are generated via distinct feedback mechanisms. The oscillation at f_{low} is achieved by introducing feedback elements into the bias circuitry. In turn, the oscillation at f_{high} relies on high-frequency series feedback and uses a stepped-impedance resonator, over which the MUT is placed. The high quality factor of this resonator enables low phase noise in the high-frequency oscillation (at f_{high}). On the other hand, achieving a low phase noise at the low-frequency oscillation (at f_{low}) is relatively undemanding. The low-frequency feedback elements are selected through a systematic procedure based on the use of stability circles and a subsequent rigorous stability analysis using pole-zero identification [27], [28]. The oscillation at f_{low} modulates the one at f_{high} and its harmonic components, generating multiple spectral lines around each harmonic, spaced by f_{low}. This self-modulated solution is efficiently analyzed using the envelope-transient method [29], which is used to demonstrate

Received 17 April 2025; revised 3 July 2025; accepted 30 July 2025. Date of publication 7 August 2025; date of current version 26 November 2025. This work was supported by the Spanish Ministry of Science and Innovation (MCIN/AEI/10.13039/501100011033) under Grant PID2020-116569RB-C31 and Grant PID2023-147653OB-C31. *(Corresponding author: Mabel Pontón.)*

The authors are with the Departamento de Ingeniería de Comunicaciones, Universidad de Cantabria, Santander 39005, Spain (e-mail: mabel.ponton@unican.es; sanchosm@unican.es; suareza@unican.es).

Digital Object Identifier 10.1109/TMTT.2025.3595262

that the two oscillations are coupled. Thus, any variation in the MUT results in a change in the modulation frequency, and consequently, in the spacing of the spectral lines. A major advantage is the low phase noise of the central frequency f_{high} and its sideband frequencies, spaced at f_{low}.

The self-modulated sensing is based on the central frequency, frequency spacing, and amplitude of the spectral lines, enhancing both sensitivity and reliability. The method provides redundancy and enables the detection of subtle variations in both the real and imaginary parts of the MUT dielectric constant. Sensing at higher order sidebands inherently increases frequency sensitivity [25] and amplitude variations across the spectral lines help detect losses and environmental influences, improving robustness against noise and other external factors.

The calibration procedure involves collecting data from reference materials with well-characterized dielectric properties [30]. For each material, the central frequency, frequency spacing, and amplitude of multiple spectral lines around a high-frequency carrier are measured. These data are used to build a calibration model that relates these spectral features to the real and imaginary parts of the MUT's dielectric constant. Once established, the model is used in the sensing phase by measuring the same spectral parameters of the unknown MUT and inputting them into the model. This multipoint sensing approach enhances sensitivity, robustness, and accuracy in material characterization. The method is demonstrated using a version of the free-running oscillator from [10] and [26], modified with additional feedback elements to produce the low-frequency oscillation. The fabricated circuit has been applied to sensing the dielectric constant of defective solid samples and detecting small volumes of ethanol in DI water.

The main contribution of this work is the proposal of a new self-modulated oscillator sensor resulting from two concurrent oscillations at high and low frequencies: f_{high} and f_{low}, generated using a single transistor device. We present a systematic design approach based on the judicious introduction of a low-frequency feedback loop into an existing high-frequency oscillator, which includes a passive resonator affected by the MUT. For the first time to our knowledge, we demonstrate the simultaneous influence of the MUT on two concurrent oscillations, coupled through the nonlinear effects of the active device, as explained using an envelope-domain formulation. The sensing relies on multiple variables that change with the MUT. This multivariable approach enables robust multipoint detection and is expected to offer higher sensitivity compared with traditional methods that rely on a single oscillation frequency and amplitude.

This article is organized as follows. Section II details the design of the self-modulated free-running oscillator. Section III presents the oscillator analysis using the envelope-transient method. Section IV describes the experimental characterization and the calibration procedure.

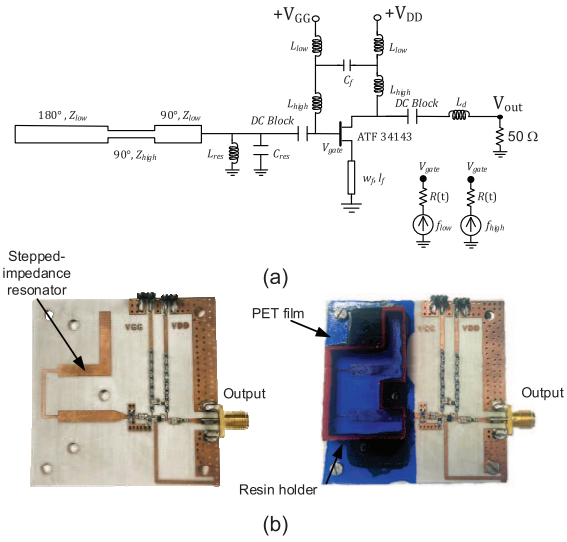

Fig. 1. Free-running oscillator taken from [10] and [26]. It is built on Rogers 4003C and based on the transistor ATF34143. The MUT is placed on a three-stage stepped impedance resonator, with Q = 485.88. (a) Schematic. (b) Photograph of the complete circuit, without and with the resin holder.

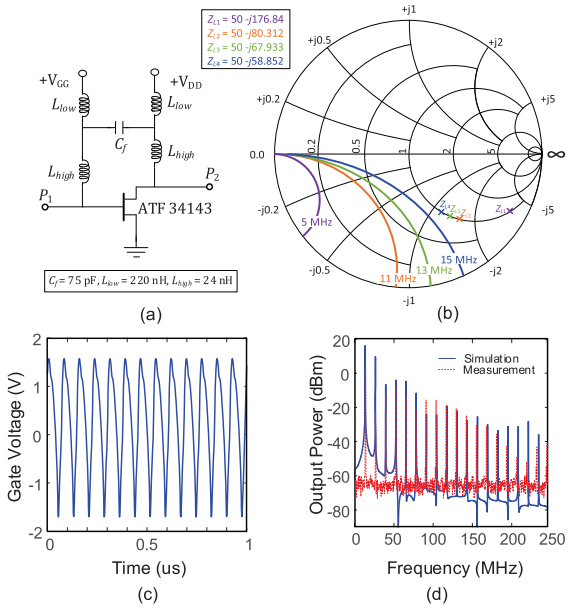

Fig. 2. Low-frequency oscillation. (a) Reduced schematic used to calculate the load stability circles. (b) Circles at 5, 11, 13, and 15 MHz. The stable region corresponds to the inside of the circles. The load impedance of the full circuit, $Z_L(f_{\text{low}})$, is also indicated. (c) Waveform of the low-frequency oscillation of a reduced circuit (described in the main text), obtained through time-domain integration. (d) Spectrum. Comparison between simulation and measurements. In the experiment we removed the high-frequency circuitry and added an 82-pF dc block.

II. Design of the Self-Modulated Free-Running Oscillator

We will consider the same free-running oscillator presented in [10] and [26], which is built on Rogers 4003C and based on the transistor ATF34143 (Fig. 1). The high-frequency oscillation is achieved through series feedback by connecting a transmission line to the source terminal. The MUT is placed on a three-stage stepped impedance resonator at the high frequency $f_{\text{high}} \cong 2.0$ GHz. This resonator has an external low-impedance section with an electric length of 180° at the desired resonance frequency, followed by a middle high-impedance section of 90° and a final low-impedance section of 90° (Fig. 1). Its quality factor is Q = 485.88, which should enable a low phase noise. In the absence of the MUT, the circuit exhibits a free-running oscillation at f_{high} = 1.99 GHz. For the self-modulated operation, we also need a low-frequency oscillation, with intended frequency, f_{low},

about 10 MHz. Because the order of magnitude of the two frequencies is quite different, we will initially perform a decoupled synthesis of the oscillation at f_{low}, by focusing on the elements with the greatest influence at low frequency [Fig. 2(a)]. The low-frequency oscillation will be achieved by connecting the feedback capacitor C_f between gate and drain. We need two distinct types of dc feeds: L_{high} and L_{low}. The inductors L_{high} should be large enough to minimize the impact of C_f at f_{high} and low enough to enable significant feedback (through C_f) at f_{low}. The inductors L_{low} (connected between the two nodes of C_f and the dc sources) must be high enough to avoid an excessive reduction of the transfer gain at f_{low}.

After the introduction of these elements, we calculate the stability circles and tune C_f, L_{high} and L_{low} to obtain a negative conductance between the gate terminal and ground around 10 MHz. This is done considering the load impedance (between the drain terminal and ground) of the full circuit, calculated at f_{low}, which is denoted as $Z_L(f_{\text{low}})$. Fig. 2(b) presents the load stability circles at 5, 11, 13, and 15 MHz, when taking C_f = 75 pF, L_{low} = 220 nH, and L_{high} = 24 nH. The stable region corresponds to the inside of the circles. The three values of $Z_L(f_{\text{low}})$, which are very similar, are also indicated, and belong to the unstable region. The source impedance of the original circuit, $Z_S(f_{\text{low}})$, calculated between the gate terminal and ground, satisfies the oscillator start-up conditions at 10.4 MHz.

For an approximate evaluation of the low-frequency oscillation, we have carried out a time-domain integration of a reduced version of the circuit, including only low-frequency components. This is necessary to prevent the start-up of the high-frequency oscillation. We have replaced the complete source and load networks with just a dc block (180 pF), connected to the gate terminal, and a dc block (180 pF) in series with the load resistor (50 Ω), connected to the drain terminal. The analysis of this reduced circuit version enables estimation of the waveform and spectrum of the low-frequency oscillation. This oscillation should exhibit significant harmonic content to give rise, in the concurrent solution, to multiple sideband components around f_{high}. As shown in Fig. 2(c), the waveform is quite irregular, exhibiting high harmonic content, as shown in Fig. 2(d). The resulting oscillation frequency is f_{low} = 12.99 MHz. For experimental verification, we removed the high-frequency circuitry and added an 82-pF dc block to prevent exceeding the maximum power limit supported by the spectrum analyzer, which is 17 dBm. The results are shown in Fig. 2(d). The fundamental frequency is practically the same (13.25 MHz in simulation, 13.11 MHz in measurement). The amplitude differences are attributed to the high-pass filtering effects of dc block.

Next, we consider the complete circuit shown in Fig. 1(a), which exhibits two different feedback mechanisms: series feedback at f_{high} and parallel feedback at f_{low}. We apply a two-stage stability analysis to verify conditions indicative of the existence of a solution with concurrent oscillations at f_{low} and f_{high}. In the first stage, we perform a rigorous stability analysis of the dc solution of the complete circuit, using pole-zero identification [27], [28]. As shown in Fig. 3, we obtain two pairs of complex-conjugate poles, at f_{low} and f_{high}, located on the right-hand side (RHS) of the complex plane. The frequencies of the poles are f_{low} = 8.3 MHz and f_{high} = 1.99 GHz. In the second stage, we calculate the periodic solution at f_{high} (in the presence of the low-frequency feedback loop) using harmonic balance (HB). We have taken f_{high} as the only fundamental frequency and considered NH =7 harmonic terms. The resulting output spectrum is shown in Fig. 4(a). Then, we perform a stability analysis of this periodic oscillation. Due to the influence of the low-frequency loop, the periodic solution at f_{high} is unstable, as desired. This has been verified applying pole-zero identification to the periodic solution at f_{high}, which requires the use of the conversion-matrix approach [27], [28]. The resulting pole locus [Fig. 4(b)] exhibits one pair of complex-conjugate poles at f_{low}, located on the RHS. The instability of the dc solution at both f_{low} and f_{high}, along with the instability of the periodic solution at f_{low}, indicates the existence of a quasi-periodic solution with two concurrent oscillations at f_{low} and f_{high}.

Due to the large difference in the time scale of the two oscillations, time-domain integration would require closely spaced samples during a long-time interval, accounting for the effect of f_{low}, which will generally be unfeasible. Alternatively, HB requires initializing both the oscillations, which can only be achieved using two auxiliary generators [31] that must be simultaneously optimized—a process that, unless the number of significant intermodulation products is low, will lead to convergence problems. As shown in Section III, the self-

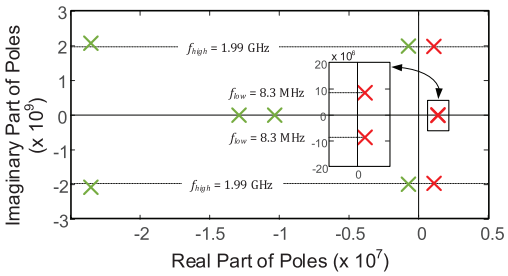

Fig. 3. Stability analysis using pole-zero identification of the dc solution of the complete circuit in Fig. 1(a), exhibiting two pairs of complex conjugate poles at f_{low} and f_{high} on the RHS.

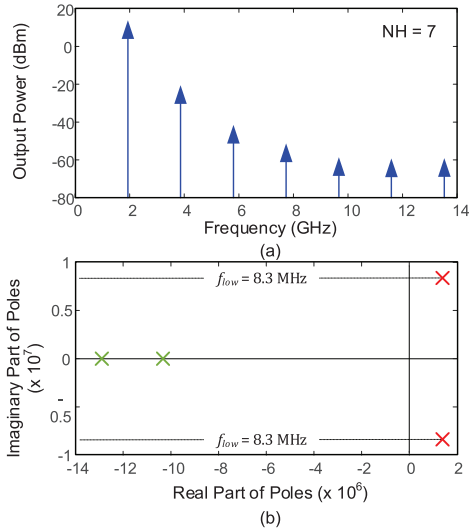

Fig. 4. Analysis of the high-frequency periodic solution, at f_{high}. (a) Periodic spectrum obtained through HB, considering NH =7 harmonic terms, in the presence of the low-frequency feedback loop. (b) Pole-zero identification applied to this periodic solution. It exhibits one pair of complex-conjugate poles at f_{low}, located on the RHS.

modulated oscillator is most accurately analyzed with the envelope-transient method.

III. Envelope-Domain Analysis of the Self-Modulated Free-Running Oscillator

The self-modulated oscillator will be analyzed with envelope transient [29], [32], [33], [34], [35], [36]. We will express the circuit variables in a Fourier series, with f_{high} as the only fundamental frequency and slowly varying harmonic terms—modulated at a rate expected to be governed by the oscillation at f_{low}. We will consider the same number of harmonic terms as in the HB analysis of Fig. 4(a), that is, NH =7. Thus, we will have

$$x(t) = X_0(t) + \sum_{k=-\text{NH}}^{\text{NH}} X_k(t)\exp(jk\omega_{\text{high}}t) \tag{1}$$

where $x(t)$ is the vector of system variables in the time domain, $X_k(t)$ is the vector composed of the kth harmonics of these variables, such that $k \neq 0$, and $\omega_{\text{high}} = 2\pi f_{\text{high}}$. The actual analyses will be carried out using nodal envelope-transient simulation [34], [35], [36]. However, for a conceptual explanation of the influence of the MUT's dielectric constant, ε_r, we make use of the piecewise approach [29], [32], [33], which facilitates understanding by clearly distinguishing between linear and nonlinear contributions. The piecewise approach [29], [32], [33] is applicable when the bandwidth of the modulation signal is significantly smaller than f_{high}. Here, this bandwidth is determined by the low-frequency oscillation at f_{low} and its harmonic content. From an inspection of Fig. 2(d), this condition is fulfilled since f_{high} = 1.992 GHz. We will also separate the matrix equation at baseband (index 0) from the matrix equation at the rest of harmonic frequencies. The full system is

$$\begin{aligned} &A(0)X_0(t) + B(0)Y_0(X(t)) + A_\omega(0)\dot{X}_0(t) \\ &\quad + B_\omega(0)\dot{Y}_0(X(t)) + D(0)G = 0 \\ &A(k\omega_{\text{high}},\varepsilon_r)X_k(t) + B(k\omega_{\text{high}},\varepsilon_r)Y_k(X(t)) \\ &\quad + A_\omega(k\omega_{\text{high}},\varepsilon_r)\dot{X}_k(t) + B_\omega(k\omega_{\text{high}},\varepsilon_r)\dot{Y}_k(X(t)) = 0 \end{aligned} \tag{2}$$

where $A(k\omega_{\text{high}},\varepsilon_r)$, $B(k\omega_{\text{high}},\varepsilon_r)$, and D are the passive linear matrices (the two first depending on ε_r), $X_0(t)$, $X_k(t)$, and $Y_0(t)$, $Y_k(t)$ are the vectors of baseband and kth harmonic components of the state variables and nonlinearities, respectively, and G is the vector of dc sources. The matrices $A(k\omega_{\text{high}},\varepsilon_r)$, $B(k\omega_{\text{high}},\varepsilon_r)$ directly affect the components $X_k(t)$ and $Y_k(X(t))$, where $k \neq 0$. In (2), the matrices are expanded in a first-order Taylor series, which is a valid approach due to the narrow modulation band. Note that the subscript ω indicates frequency derivative. The multiplication by the frequency increment $j\Delta\omega$ acts like a time differentiator [29], [32], [33]. This gives rise to the differential equation system in the slowly varying envelopes of the state variables $X_0(t)$ and $X_k(t)$, shown in (2).

Because (2) is an autonomous equation system, an initial condition is required to initialize the oscillations. Otherwise, it will converge to the unstable dc solution. To obtain the quasi-periodic solution with concurrent oscillations, we must provide initial conditions at both f_{low} and f_{high}. This is done by introducing current sources of small amplitude at the two frequencies [Fig. 1(a)], which are connected to the circuit during the initial time steps only. The low-frequency oscillation

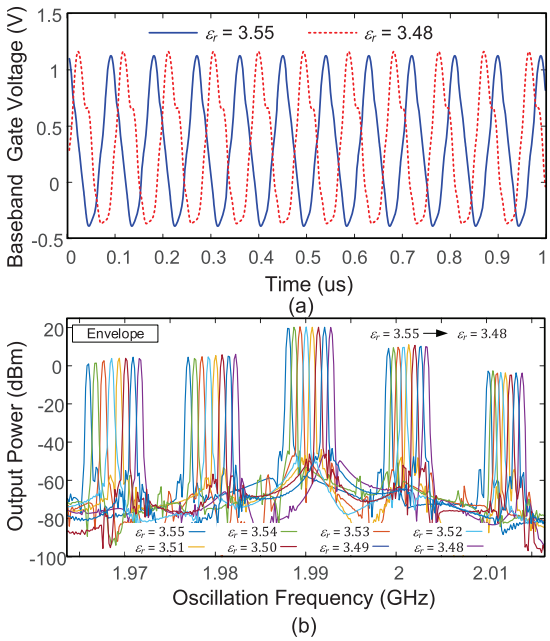

Fig. 5. Envelope-transient simulation of the concurrent oscillator in Fig. 1. (a) Baseband oscillation when placing an MUT with ε_r = 3.55 and ε_r = 3.48 over the stepped-impedance resonator. (b) Spectra about the high-frequency carrier when varying ε_r from 3.55 to 3.48.

gives rise to a baseband term $X_0(t)$, at the frequency f_{low} (in steady state), which impacts the full vector $X(t)$ through the nonlinear dependences of $Y(X(t))$ and $\dot{Y}(X(t))$. Due to the harmonic mixing, all the terms of Y and $\dot{Y}$ depending on $X_0(t)$ become time-varying. Moreover, the need to fulfill the nonlinear system (2) will give rise to the time variation in all the components of the vector $X(t)$ at the rate of f_{low}. Because the baseband term $Y_0(X(t))$ depends on the full vector $X(t)$, any variation in ε_r, affecting the high-frequency components, will have an impact on the oscillation at f_{low} and, therefore, on the spacing of the spectral lines about kf_{high}. This is because, as explained, the two subsets of equations in (2) are coupled through the nonlinear terms.

We have performed an envelope-transient analysis of the circuit in Fig. 1 when placing a solid material over the stepped-impedance resonator, acting like the MUT. As stated, the analysis relies on a nodal envelope-transient formulation. We have considered a very small variation in the dielectric constant, from ε_r = 3.55 to ε_r = 3.48, which will be implemented in the experiment by drilling holes in the material (defective samples). The baseband voltage waveforms at the gate node obtained for ε_r = 3.55 and ε_r = 3.48 are compared in Fig. 5(a). For ε_r = 3.55, we have f_{low} = 11 MHz and f_{high} = 1.988 GHz. For ε_r = 3.48, we have f_{low} = 10.1 MHz and f_{high} = 1.992 GHz. Thus, the MUT influences both the low- and high-frequency oscillations.

We have also analyzed the modulated high-frequency oscillation. Fig. 5(b) presents the output spectra about f_{high}, obtained when varying the MUT dielectric constant from ε_r = 3.55 to ε_r = 3.48. Note that both the real and imaginary parts of all the circuit variables in (1) become modulated by the oscillation at ω_{low}. Thus, the envelope $V_{\text{out}}(t)$ is a complex number, so its spectrum is nonsymmetrical about ω_{high}.

As seen in Fig. 5(b), the lowest sideband spectral lines exhibit the highest frequency sensitivity. To understand this,

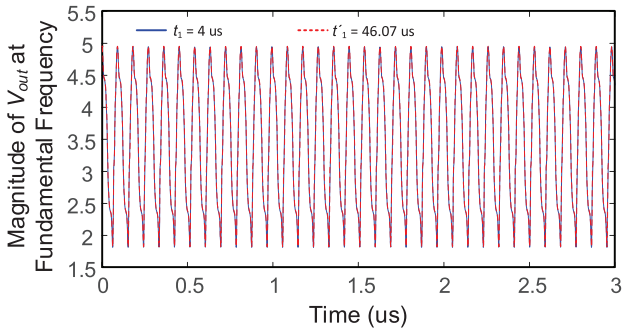

Fig. 6. Demonstration of permanent behavior. We have performed two envelope-transient simulations. In the first one, we display the output-voltage waveform about f_{high} from $t_1 = 4$ μs to $t_2 = 10$ μs. In the second simulation, we display data from $t_1 = 46.07$ μs to $t_2 = 52.07$ μs. The same waveform (though time shifted) is obtained.

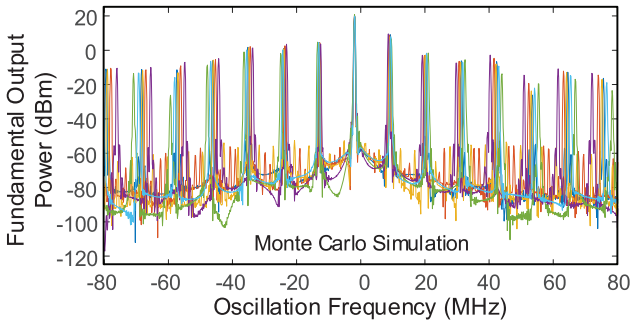

Fig. 7. Monte Carlo simulation when considering tolerances of 2% in the elements of the low-frequency feedback loop: C_f, L_{high}, L_{low}. The output spectra corresponding to each trial are shown.

we must note that the spectral lines are located at

$$\begin{aligned} f_{k,-m} &= kf_{\text{high}}(\varepsilon_r) - mf_{\text{low}}(\varepsilon_r) \\ &\cdots \\ f_{k,-1} &= kf_{\text{high}}(\varepsilon_r) - f_{\text{low}}(\varepsilon_r) \\ f_{k,0} &= kf_{\text{high}}(\varepsilon_r) \\ f_{k,1} &= kf_{\text{high}}(\varepsilon_r) + f_{\text{low}}(\varepsilon_r) \\ &\cdots \\ f_{k,m} &= kf_{\text{high}}(\varepsilon_r) + mf_{\text{low}}(\varepsilon_r) \end{aligned} \tag{3}$$

where k is the harmonic of the high-frequency oscillation and m is a positive integer. Under the same variation in the MUT dielectric constant (from ε_r to ε'_r), the positive $(+m)$ and negative $(-m)$ spectral lines about kf_{high} will undergo a shift Δf_m, Δf_{-m} given by

$$\begin{aligned} \Delta f_m\left(\varepsilon'_r, \varepsilon_r\right) &= k\left[f_{\text{high}}\left(\varepsilon'_r\right) - f_{\text{high}}\left(\varepsilon_r\right)\right] \\ &\quad + m\left[f_{\text{low}}\left(\varepsilon'_r\right) - f_{\text{low}}\left(\varepsilon_r\right)\right] \\ &= k\Delta f_{\text{high}}\left(\varepsilon'_r, \varepsilon_r\right) + m\Delta f_{\text{low}}\left(\varepsilon'_r, \varepsilon_r\right) \\ \Delta f_m\left(\varepsilon'_r, \varepsilon_r\right) &= k\left[f_{\text{high}}\left(\varepsilon'_r\right) - f_{\text{high}}\left(\varepsilon_r\right)\right] \\ &\quad - m\left[f_{\text{low}}\left(\varepsilon'_r\right) - f_{\text{low}}\left(\varepsilon_r\right)\right] \\ &= k\Delta f_{\text{high}}\left(\varepsilon'_r, \varepsilon_r\right) - m\Delta f_{\text{low}}\left(\varepsilon'_r, \varepsilon_r\right). \end{aligned} \tag{4}$$

Depending on the signs of Δf_{high} and Δf_{low}, either the positive or negative spectral lines will undergo a larger shift than Δf_{high}, which is similar to the one obtained in the absence of the low-frequency feedback loop. Thus, the self-modulated oscillator sensor intrinsically offers enhanced sensitivity compared with its nonmodulated counterpart. In the case of the circuit in Fig. 1, when reducing ε_r we have both $\Delta f_{\text{high}} < 0$ and $\Delta f_{\text{low}} < 0$. Thus, the negative spectral lines should be more sensitive to the MUT than the positive ones, as is clearly observed in Fig. 5(b). We note a significant sensitivity of f_{low} to the MUT. For $\varepsilon_r = 3.55$, we have $f_{\text{low}} = 11$ MHz, whereas for $\varepsilon_r = 3.48$ we obtain $f_{\text{low}} = 10.1$ MHz, so the increment is $\Delta f_{\text{low}} = -0.9$ MHz.

To rigorously validate permanent behavior, we have performed two envelope-transient simulations. In the first one, we display the output-voltage waveform about f_{high} from $t_1 = 4$ μs to $t_2 = 10$ μs. In the second simulation, considering a much longer time interval, we display data from $t_1 = 46.07$ μs to $t_2 = 52.07$ μs. Fig. 6 shows the waveform of the envelope about the fundamental frequency at the output node. As can be seen, the same waveform (though time-shifted) is obtained.

We have also performed a Monte Carlo analysis to evaluate the effects of variations in the bias circuit components. We have considered tolerances of 2% in the elements of the low-frequency feedback loop: C_f, L_{high}, and L_{low}, which provides the results in Fig. 7. However, the actual fabricated circuit will have fixed component values, so variations will primarily arise from aging or degradation. While a 2% variation is relatively large—especially when using high-quality components from Coilcraft and ATC, as in this case—the analysis helps illustrate the potential impact of such variations on the spectrum. The amplitude variation also increases with m, as higher order lines span a broader frequency range and are therefore more affected by the frequency-dependent behavior of both the reactive elements and the active device.

IV. Sensor Operation

In this section, we present the experimental validation of the theoretical analysis from Section III, along with the sensing procedure based on multivariable calibration. Initially, we will use solid materials to establish baseline performance. Then, we will address the case of liquid mixtures.

A. Experimental Characterization

For the experimental characterization, we have used the setup shown in Fig. 8. As stated, the oscillator in Fig. 1 is built on Rogers 4003C and based on the ATF34143 transistor. It is connected to an R&S FPL Spectrum Analyzer through the 10-dB coupled port of a directional coupler to protect the analyzer's maximum power limit of 17 dBm. Simultaneously, the phase-noise spectral density is monitored using an R&S FSWP8 Phase Noise Analyzer connected to the direct port of the directional coupler. The oscillator is biased using the low-noise power supplies integrated into the R&S FSWP8.

Initially, we considered the transistor bias point $V_{GG} = -0.1$ V and $V_{DD} = 3$ V (consumption 52 mW), and performed a sensing of defective solid samples. These are placed on the stepped-impedance resonator. The position and height of the MUT influence the sensor's response. Thus, it is important that the MUT's height remains constant, as it affects the electromagnetic coupling with the resonator. The sample position, on the other hand, is fixed using mechanical screws that securely hold each sample in place.

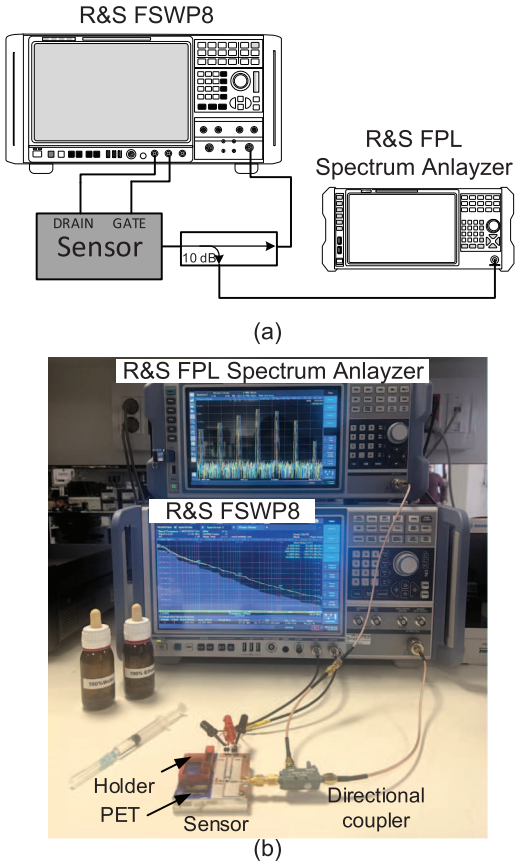

Fig. 8. Experimental setup. (a) Sketch. The output port of the oscillator in Fig. 1 is connected to an R&S FPL Spectrum Analyzer through the 10-dB coupled port of a directional coupler. Simultaneously, the phase-noise spectral density is monitored using an R&S FSWP8 Phase Noise Analyzer connected to the direct port of the directional coupler. The oscillator is biased using the low-noise power supplies integrated into the R&S FSWP8. (b) Photograph.

To induce a small reduction in the MUT dielectric constant, we drilled holes in a layer of Rogers 4003C, with $\varepsilon_r = 3.55$. The resulting dielectric constant is estimated using the approximate expression in [37] and [38]

$$\varepsilon_r = \varepsilon_{r,s} \frac{1 + 2V_F \frac{1-\varepsilon_r}{1+2\varepsilon_r}}{1 - V_F \frac{1-\varepsilon_r}{1+2\varepsilon_r}} \tag{5}$$

where $\varepsilon_{r,s}$ is the dielectric constant of the intact material and V_F is the volumetric fraction of air in the material, which changes with the radium and/or number of the holes. The aim is to obtain ε_r values comprised between $\varepsilon_r = 3.55$ and $\varepsilon_r = 3.50$, which represents a tiny variation interval. Note that as in most previous works dealing with solid structures [1], [2], [3], [4], [5], we neglect the variation in the imaginary part. Instead, this variation will be considered in the second experiment, devoted to liquid sensing. The relevant parameters to calculate (5) are the numbers of holes and their size. To achieve $\varepsilon_r = 3.5$, we drilled a sample of Rogers 4003C substrate with a nominal dielectric constant $\varepsilon_{r,s} = 3.55$. The sample has an area of 217.6 mm^2 and a thickness of 0.8128 mm resulting in a total volume $V_{\text{total}} = 176.99$ mm^3. A total of 26 circular holes with a radius of 0.2 mm were drilled through the substrate. The volume of each hole is $V_{\text{hole}} \cong 0.102$ mm^3. Therefore, the total volume of air due to the holes is $V_{\text{holes}} \cong 2.657$ mm^3.

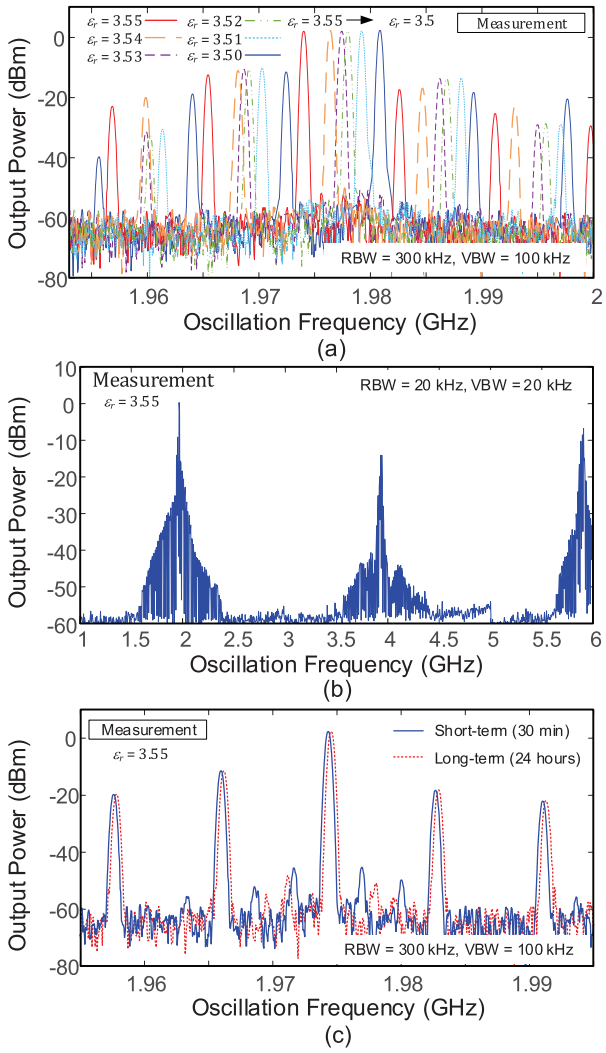

Fig. 9. Sensing of defective materials. Experimental spectra obtained considering a solid material in which holes are drilled, giving rise to a reduction of ε_r from 3.55 (no holes) to 3.5. (a) Spectrum in the interval 1–2 GHz. (b) Spectrum obtained for $\varepsilon_r = 3.55$ in the interval 1–6 GHz. (c) Comparison of the spectrum for $\varepsilon_r = 3.55$ after 30 min since bias turn-on with the spectrum after 24 h.

This results in a volumetric air fraction $V_F \cong 0.0150$. Using approximation (5), the effective dielectric constant is $\varepsilon_r \cong 3.5$.

Next, we present the spectrum variations observed with the defective material samples. Multiple measurements were performed for each sample, and the central frequency, frequency spacing, and spectral line amplitude were found to be highly stable across trials. To assess consistency, each sample was placed three times. In addition, removing and reattaching the screws nine times resulted in a maximum frequency variation of 150 kHz and a maximum amplitude variation of 0.004 dB. Fig. 9(a) shows the experimental results when reducing ε_r from 3.55 to 3.5. As can be seen, a small change in ε_r leads to a significant variation in the central frequency, frequency spacing, and amplitudes of the spectral lines. We have $\Delta f_{\text{low}} < 0$, so the spectral lines $f_{\text{high}}(\varepsilon_r) - mf_{\text{low}}(\varepsilon_r)$ with the highest m exhibit the greatest sensitivity, in agreement with the analysis predictions. There is good agreement between measurements and simulations in terms of the two oscillation frequencies and the output power (note that the experimental

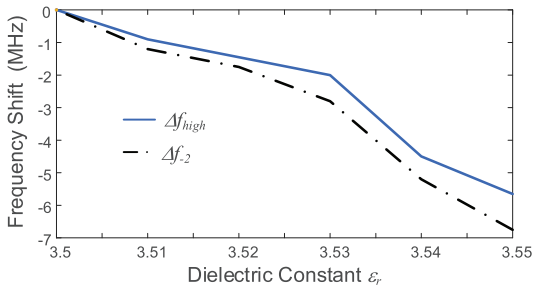

Fig. 10. Sensing of defective materials when varying ε_r from 3.5 to 3.55. Experimental evolution versus ε_r of the frequency increment of the central spectral line, Δf_{high}, and the sideband, Δf_{-2}.

output power is attenuated by the coupler). However, the sensitivity is higher in the experiment, which is attributed to tolerances in the transistor and other components, and several modeling limitations. Instead of using an electromagnetic simulation, which would be computationally costly, we modeled the transmission line with the MUT on top using effective dielectric constant approximation [37], [38]. Another assumption was the calculation of the dielectric constant of the defective substrates using the approximate expression (5). In the experimental spectra of Fig. 9(a), very good sensitivity is obtained for $m = 2$, with the frequency varying in 6.75 MHz when ε_r is changed from 3.55 to 3.5. Fig. 9(b) shows a broader view of the output spectrum obtained for $\varepsilon_r = 3.55$ in the interval of 1–6 GHz.

We have also performed time-based measurements to demonstrate the persistence and reliability of the quasi-periodic solutions. There will be a drift caused by temperature-dependent variations in the transistor's characteristics, such as junction capacitance and gain, which affect the oscillator's stability. There will also be changes in the passive components, particularly capacitors and inductors whose values can shift with temperature, voltage, and aging. Power supply fluctuations can also alter the transistor's operating point, leading to frequency shifts. We compared the output spectrum after 30 min since bias turn-on with the spectrum after 24 h. It is important to note that the experiment was not conducted under temperature-controlled conditions; instead, the circuit was left to operate under the ambient laboratory environment. The results for $\varepsilon_r = 3.55$ are shown in Fig. 9(c). We would like to emphasize that a conventional periodic oscillator sensor suffers from the same problem. The frequency drift after operation for 24 h is about 150 kHz in the main spectral line for both the periodic and quasi-periodic spectra. Note that this drift is the dominant one in the quasi-periodic case and causes approximately the same shift in all the spectral lines of the self-modulated solution.

For a more detailed characterization, Fig. 10 shows comparison of the variation in the frequency increment Δf_{high} and the frequency increment $\Delta f_{\text{high}} - 2\Delta f_{\text{low}}$ when changing ε_r from 3.55 to 3.5. As expected, this lower sideband frequency exhibits a higher sensitivity. We have also analyzed the spectrum about the harmonic $3f_{\text{high}}$ for $\varepsilon_r = 3.55$, 3.52 and 3.50. Simulations and measurements are shown in Fig. 11(a) and (b), respectively. In agreement with (4), the shift Δf_{high} of the fundamental frequency results in a shift of $3\Delta f_{\text{high}}$ at the third harmonic. The spectral lines about each shifted harmonic vary as $3\Delta f_{\text{high}}(\varepsilon_r', \varepsilon_r) \pm m\Delta f_{\text{low}}(\varepsilon_r', \varepsilon_r)$. We conclude that,

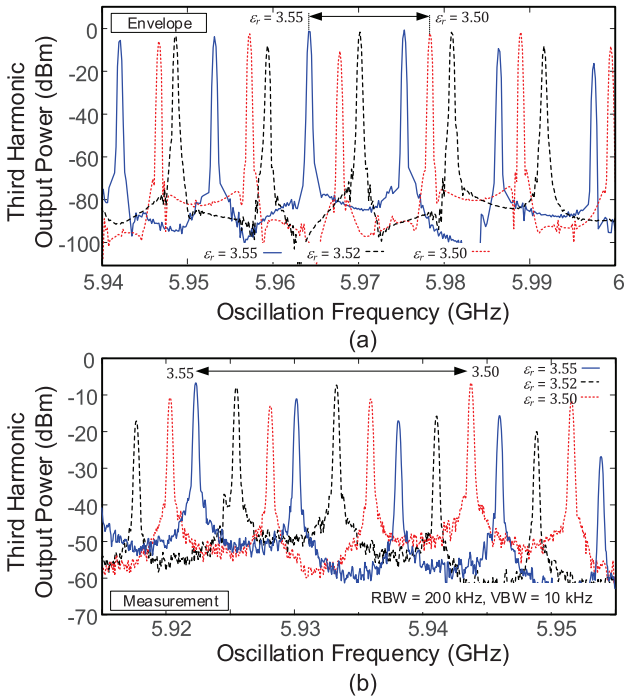

Fig. 11. Spectrum about the third harmonic of the high-frequency oscillation, $3f_{\text{high}}$ ($k = 3$). (a) Simulation. (b) Measurements.

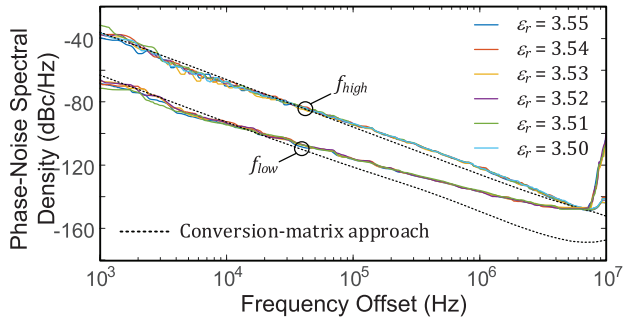

Fig. 12. Sensing of defective materials. Experimental variation in the phase-noise spectral density at both f_{high} and f_{low} when ε_r is changed from 3.55 to 3.5. The results are compared with those obtained in simulation. They have been achieved by sequentially initializing the two distinct periodic solutions, at f_{high} and f_{low}, in HB, and applying the conversion-matrix approach.

provided the amplitudes are high enough, a simple way to increase sensitivity is to perform the detection about a higher harmonic term.

Low phase noise is a key objective of this work, as it ensures robustness and reliability in the sensing process. It has been characterized using the R&S FSWP8 Phase Noise Analyzer. Initially, we captured the spectral line with the highest output power, which corresponds to the carrier frequency f_{high}. The collection of experimental phase-noise spectra obtained when varying ε_r from 3.55 to 3.5 is shown in Fig. 12. As can be seen, the phase-noise variations are small, and the spectral density at 100 kHz is −94 dBc/Hz. Next, we have searched for the spectral line corresponding to the low-frequency oscillation at f_{low}, by requesting a phase-noise measurement at about 8 MHz. The resulting collection of phase-noise spectra is also shown in Fig. 12. The phase noise at f_{low} is significantly lower than at f_{high}. This is because the oscillator's ability to

TABLE I
SENSITIVITY COMPARISON FOR SOLID MATERIALS

Ref.	$\Delta\varepsilon_r$	Δf(MHz)	Resonance Frequency (GHz)	Resonator	Linearity RMSE (MHz^2)	$\varepsilon_{r,\max}-\varepsilon_{r,\min}$ for linearity calculation
[10]	0.05	2.8	2.40	Stepped-impedance	1.369×10^{0}	5.7
[10]	0.05	6.4	2.40	Slow-wave structure	6.055×10^{0}	5.7
[44]	0.05	7.6	4.62	Complementary split-ring	1.553×10^{1}	7.45
[45]	0.05	---	2.18	Magnetic LC	7.525×10^{1}	9.5
[46]	0.05	10	5.95	Complementary split-ring	8.566×10^{1}	9.3173
[47]	0.05	---	2.47	Complementary split-ring	8.707×10^{1}	4.6531
Keysight N1501A Probe Kit (Commercial)	0.05	~3.5	10	Coaxial dielectric probe	~1.0	Standard VNA-based dielectric sensing
Rohde & Schwarz ZNB + Dielectric Kit	0.05	~4.2	8	Resonant cavity sensor	~0.8	High precision permittivity measurement
This work	**0.05**	**5.65 (Δf_o) 6.75 (Δf_{-2})**	**2.00**	**Stepped-impedance**	**6.405×10^{-1}**	**0.05**

suppress noise decreases with higher f_o unless its quality factor is proportionally increased [39], [40]. Second, the conversion of timing jitter to phase jitter becomes more severe at higher frequencies, since a fixed amount of time uncertainty results in larger radian phase deviations as frequency increases. Finally, the active device contributes more noise at higher frequencies because its gain drops and its noise figure rises closer to its transit frequency limits. Due to the difficulty in the harmonic-balance simulation of the double autonomous quasi-periodic solution (with two concurrent oscillations), we have separately analyzed the phase noise of the high-frequency and low-frequency oscillations. This has been done by sequentially initializing the two distinct periodic solutions, at f_{high} and f_{low}, in HB. The phase-noise spectrum of each periodic solution has been calculated using the conversion-matrix approach [41]. The periodic analyses help justify the low phase noise observed experimentally, though we are aware that the results should differ from those obtained with the concurrent solution due to the coupling between the two oscillations. For instance, the phase-noise analysis of the periodic oscillators is unable to detect the increment of spectral density due to the presence of the next spectral line. This is observed in the experimental spectrum at both f_{high} and f_{low}, as shown in Fig. 12. With respect to its impact on the sensing accuracy, we must note that phase noise does not shift the carrier frequency—that is, the central frequency of the spectrum [41], [42], [43]. However, the resulting spectral broadening degrades the ability to accurately measure small frequency shifts and amplitude variations, which directly impacts the resolution and sensitivity of the system. Nevertheless, the well-defined and reproducible spectra, obtained under small MUT variations, confirm that the system remains robust even in the presence of moderate noise.

Table I shows comparison of the frequency sensitivity and linearity with those of other material sensors recently presented in the literature. Linearity is calculated based on the root mean square error (RMSE) deviation from an ideal linear variation. The works included share a common feature: they rely on the detection of frequency shifts as the sensing mechanism—on which our sensor is based—rather than on phase variations, for instance. Our objective was to provide a consistent benchmark by comparing the frequency shift induced by a standardized change in the dielectric constant ($\Delta\varepsilon_r = 0.05$) of a solid measurand. The table includes both passive and active sensors and shows comparison of frequency variations for $\Delta\varepsilon_r = 0.05$. Note that the main goal of this work is to show the increased sensing capabilities of self-modulated oscillators in comparison to a periodic free-running oscillator. We believe that higher sensitivities could be obtained with other oscillator designs, based on other kinds of resonators. We must also emphasize that as shown in our next experiment, the sensing here is based on a multivariable input.

The second experiment illustrates the capabilities for liquid sensing. We have sensed mixtures of ethanol and DI water. A resin holder was fabricated using a 3-D printer and sealed with epoxy glue and screws [Fig. 1(c)]. To prevent possible absorption by the substrate, a PET film was placed over the sensing area. The positioning tolerance of the MUT relative to the resonator was minimized using a fixed sample holder, which was glued directly onto the transmission line to ensure consistent coupling and prevent any displacement during measurement. Due to the impact of the holder, a change in the bias voltage was necessary, which is now $V_{GG} = -0.5$ V, $V_{DD} = 3.5$ V. Small volumes of ethanol were incrementally introduced into the holder using a syringe. We added drops of ethanol with a volume of 0.0125 mL in a volume of 2 mL of DI water. This resulted in an approximate change in the complex dielectric constant from $\varepsilon_M = 80 - j8$ (pure DI water) to $\varepsilon_M = 78.29 - j8.005$ after the addition of four drops of ethanol [48]. The same solution was measured multiple times after repositioning the probe. The spectrum evolution when adding these four drops (five samples) is shown in Fig. 13(a). As can be observed, the lower sideband frequencies exhibit the greatest variation, and the spectral lines show different amplitude sensitivities. For comparison, Fig. 11(b) shows the variation in the reflection coefficient of the passive resonator, exhibiting a lower sensitivity. The difference is due to the

TABLE II
OSCILLATOR SENSOR COMPARISON

Ref.	Frequency [GHz]	Passive Sensing Element	Sensitivity [MHz]$^{+}$	Linearity RMSE*[MHz]	Phase-noise [dBc/Hz]‡
[6]	2.00	Split-ring resonator (SRR)	1.28 (0.08%)	5.91×10^{0}	No datum
[7]	2.04–2.055	T-shaped distributed resonator	0.5	1.05×10^{2}	No datum
[49]	2.48	SRR	0.148	1.25×10^{0}	-130
[50]	2.26–2.35	Modified SRR	3.5	9.8×10^{2}	No datum
[51]	2.51–2.55	Interdigital capacitor and traveling-wave loop-directional filter	3.9	6.23×10^{1}	−128.87 −128.39
[52]	1.512–1.516	Asymmetric coplanar waveguide	0.33	1.48×10^{1}	No datum
This work	**2.00**	**Stepped-impedance resonator**	**1.1** (Δf_0) (2.44%) **1.3** (Δf_{-2}) (2.44%)	$\mathbf{1.76\times10^{-2}}$	**-127**

$^{+}\Delta f$ *@ 10% ethanol volume in the mixture*
**Root Mean Square Error*
‡ *1MHz offset frequency*

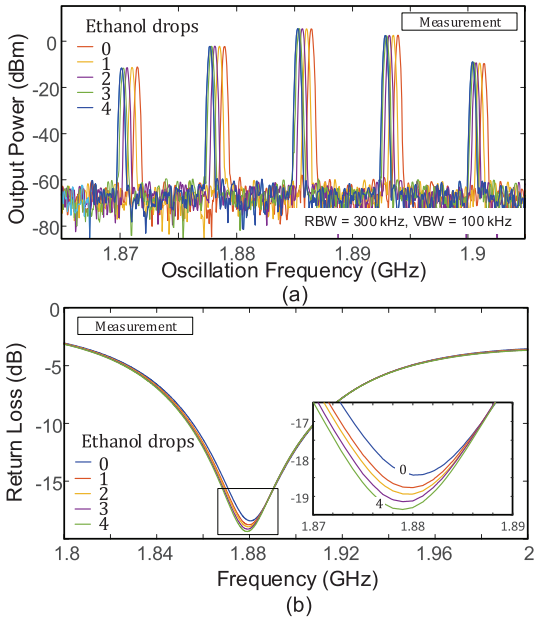

Fig. 13. Liquid sensing. Experimental spectra obtained when adding drops of ethanol with a volume of 0.0125 mL in a volume of 2 mL of DI water. (a) Spectrum of the self-modulated oscillator. (b) Return loss of the passive resonator when adding the drops.

frequency dependence of both the real and imaginary parts of the admittance exhibited by the nonlinear block containing the active device, along with the feedback and output elements. The collection of experimental phase-noise spectra obtained when adding one to four ethanol drops (five samples) is shown in Fig. 14. As can be seen, the phase-noise variations are small, and the spectral density at 100 kHz is −104 dBc/Hz.

Table II presents an additional comparison to the state of the art, focusing on oscillator-based sensors used for detecting ethanol–water mixtures. The table considers the operating frequency, sensitivity, linearity, phase noise, and type of

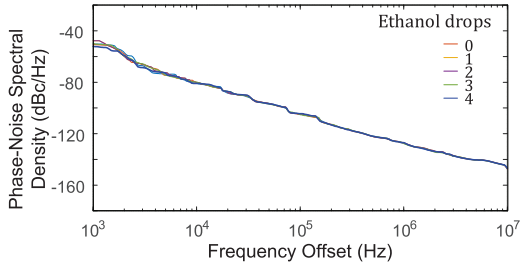

Fig. 14. Liquid sensing. Experimental variation in the phase-noise spectral density when adding one to four drops of ethanol with a volume of 0.0125 mL in a volume of 2 mL of DI water.

passive component used as the sensing element within the oscillator circuit. Sensitivity is defined as the frequency change resulting from a variation in ethanol concentration from 0% to 10%. Note that the sensitivity of the self-modulated oscillator sensor is enhanced by the collaborative action of multiple spectral lines, which is a key advantage of this implementation.

B. Calibration and Detection Procedure

For the sensing procedure, the goal is to derive a function that relates the components of the complex dielectric constant with the measured spectrum of the output signal around f_{high}. This spectrum agrees with that of the output-voltage component $v(t) = 2\text{Re}\{V_{\text{out}}(t)e^{j2\pi f_{\text{high}}t}\}$. Here, we will derive a function that relates the real and imaginary parts the complex dielectric constant with the experimental spectrum of $v(t)$, which can be expressed as

$$v(t) = \sum_{q=-Q}^{Q} A_i e^{j(2\pi f_q t+\varphi_q)} \tag{6}$$

where for $q > 0 (q < 0)$, A_q, φ_q, and f_q denote, respectively, the magnitude, phase, and frequency of the qth spectral line higher (lower) than $f_0 = f_{\text{high}}$. In the sensing procedure, we

TABLE III
MATRIX OF REGRESSION COEFFICIENTS

	ε_r	$\varepsilon_{r,I}$
1 (Intercept)	$-0.357\cdot10^4$	18
f_{-2} (GHz)	$-1.3759\cdot10^4$	39
f_{-1} (GHz)	$1.5604\cdot10^4$	-45
A_0(V)	3.3	-0.01

consider the magnitudes and frequencies of the spectral lines of $v(t)$ as input variables, collected in the row vector $u = (f_{-2}, f_{-1}, A_0)$. Then, expressing the complex dielectric constant as $\varepsilon_M = \varepsilon_r - j\varepsilon_{r,I}$, we will relate the parameters $y = (\varepsilon_r, \varepsilon_{r,I})$ to the input variables in u through the following linear regression model [28] as

$$y = x\beta + \rho \tag{7}$$

where $x = (1, u)$, β is the matrix of regression coefficients, with order 4×2, and the row vector $\rho = (\rho_1, \rho_2)$ contains the error terms. Note that the first component of the row vector x is set to 1 to allow the inclusion of a constant term in the linear model, called intercept [28]. To calibrate the model, the coefficients of matrix β are fit from a set of p measured spectra for which $(\varepsilon_r, \varepsilon_{r,I})$ are known.

In this procedure, the components of β are optimized to minimize the squared error function

$$H(\beta) = \sum_{i=1}^{p} |y_i - x_i\beta|^2 \tag{8}$$

where x_i, y_i, for $i = 1, \ldots, p$ are the values of the input and output vectors x and y for each measured spectrum. Thereafter, the matrix β can be used to estimate the dielectric parameters from the input variables u resulting from any measured spectrum as

$$\widehat{y} = x \cdot \beta \tag{9}$$

where $\widehat{y} = (\hat{\varepsilon}_r, \hat{\varepsilon}_{r,I})$ are the estimated components of the dielectric constant.

As an example, the model has been calibrated with the spectra represented in Fig. 13, which correspond to $p = 5$ values of $V_F = V_{\text{Eth}}/V_T$, where V_{Eth} and V_T are the volume of ethanol and the total volume, respectively. First, the regression coefficients that define the fit model (9) have been obtained and are shown in Table III. Each cell (i, j) corresponds to the component $\beta_{i,j}$ of the matrix of regression coefficients β. The input and output variables related by these coefficients are also indicated in the table.

Then, we have applied system (9) to estimate the components of the dielectric constant. The results are shown in Fig. 15, where the calibration samples, using data from [48], have been represented with circles. The estimated values have been marked with crosses and show very good agreement with the measured values, represented with squares. For comparison, the values estimated measuring the reflection coefficient and using both the frequency and the value of the minimum return loss as sensing parameters have been superimposed using diamond markers. We applied in both the cases an analogous calibration method. As can be seen, the accuracy is significantly lower than that of the self-modulated oscillator sensor.

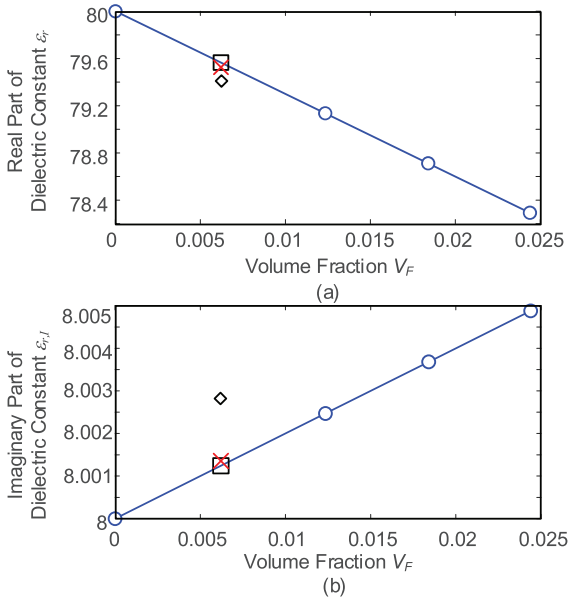

Fig. 15. Prediction of the real and imaginary parts of the dielectric constant versus variations in the fraction of ethanol in water. (a) Real part. (b) Imaginary part.

TABLE IV
TECHNICAL SPECIFICATIONS AND PERFORMANCE INDICATORS OF THE PROPOSED SENSOR

Parameter	Value	Note
Operating frequencies	~ 2.0 GHz / ~ 10 MHz	f_{high} / f_{low}
Sensitivity	**Liquids:** Δf_0 = 1.1 MHz Δf_{-2} = 1.3 MHz **Solids:** Δf_0 = 5.65 MHz Δf_{-2} = 6.75 MHz	Liquids: 2.44% ethanol in DI water Solid materials: $\Delta\varepsilon_r = 0.05$
Footprint	60 × 60 mm^2	PCB layout
Power consumption	**Liquids:** 59 mW **Solids:** 52 mW	Steady-state quasiperidic regime
Extraction error	**Liquids:** 1.76×10^{-2} **Solids:** 6.405×10^{-1}	RMSE Liquids: 2.44% ethanol in DI water Solid materials: $\Delta\varepsilon_r = 0.05$
Resonator type	Stepped-impedance	Transmission line resonator
Resonance frequency	~ 2.0 GHz	Fundamental mode
Technology	Hybrid (based on pHEMT ATF34143)	Microstrip lines and SMD discrete components
Phase-noise	**Liquids:** -127 dBc/Hz **Solids:** -122 dBc/Hz	1 MHz offset from f_{high} ~ 2.0 GHz

The statistical performance of the regression model has been analyzed by obtaining, on one hand, the coefficient of determination R^2, which quantifies how well the model explains the variance in the data, given by

$$R^2 = 1 - \frac{H(\beta)}{\sum_{i=1}^{p} |y_i - \bar{y}|^2} = 0.9991 \tag{10}$$

where $H(\beta)$ is the error function (8) and $\bar{y}$ is the mean value of the output data. The result $R^2 \simeq 1$ indicates that the fit

model explains nearly all variability in y. On the other hand, the RMSE of the predictions on the calibration set has been calculated for each component of the dielectric constant

$$\text{RMSE}_r = \sqrt{\frac{1}{p}\sum_{i=1}^{p} e_{i,r}^2} = 0.0176$$
$$\text{RMSE}_I = \sqrt{\frac{1}{p}\sum_{i=1}^{p} e_{i,I}^2} = 5.0413 \cdot 10^{-5} \quad (11)$$

where $e_i = y_i - x_i\beta = (e_{i,r}, e_{i,I})$ are the residuals of the estimation of each component of ε_M. The small RMSE values relative to the values of the components of ε_M (see Fig. 15) indicate high confidence in material identification and characterization.

Finally, Table IV summarizes the main technical specifications and performance indicators of the proposed sensor.

V. Conclusion

In this work, a novel oscillator-based sensor architecture has been presented, based on a self-modulated free-running oscillator with two concurrent high- and low-frequency oscillations. Unlike previous approaches, the proposed circuit operates in a doubly autonomous quasi-periodic regime. The design is based on the inclusion of a low-frequency loop in an existing high-frequency oscillator. The two distinct oscillations result from two different feedback mechanisms. The high oscillation frequency is determined by a stepped-impedance resonator, over which the MUT is placed. The use of this resonator enables a low phase-noise spectral density. As demonstrated through an envelope-transient analysis, the high- and low-frequency oscillations are coupled, so any change in the MUT affects the two independent frequencies. The interaction between the two oscillations produces numerous sidebands around the high-frequency carrier, with their spacing and amplitudes varying according to the properties of the MUT. This multidimensional sensing mechanism enhances both sensitivity and robustness, enabling the detection of subtle changes in the real and imaginary components of the MUT's dielectric constant. The approach has proven effective in sensing small variations in the dielectric constant in solid materials and small volumes of ethanol in DI water. The novel architecture demonstrates potential for high-resolution, noise-resilient sensing applications.

References

[1] F. Martín, P. Vélez, J. Muñoz-Enano, and L. Su, *Planar Microwave Sensors*. Hoboken, NJ, USA: Wiley, 2022.

[2] P. Casacuberta et al., "Sensitivity optimization in single-frequency planar microwave sensors for solid and liquid characterization and microfluidics," *IEEE Trans. Microw. Theory Techn.*, vol. 73, no. 3, pp. 1581–1609, Mar. 2025, doi: 10.1109/TMTT.2024.3452433.

[3] H. Yu, X. Ding, J. Chen, S. Sabbaghi, and Q. J. Gu, "Design and analysis of a sub-THz resonator-based high-resolution permittivity sensor," *IEEE Trans. Microw. Theory Techn.*, vol. 72, no. 5, pp. 2809–2823, May 2024.

[4] A. Ebrahimi and K. Ghorbani, "High-sensitivity detection of solid and liquid dielectrics using a branch line coupler sensor," *IEEE Trans. Microw. Theory Techn.*, vol. 71, no. 12, pp. 5233–5245, Dec. 2023.

[5] Z. R. Omam, V. Nayyeri, S.-H. Javid-Hosseini, and O. M. Ramahi, "Simple and high-sensitivity dielectric constant measurement using a high-directivity microstrip coupled-line directional coupler," *IEEE Trans. Microw. Theory Techn.*, vol. 70, no. 8, pp. 3933–3942, Aug. 2022.

[6] S. Mohammadi, K. K. Adhikari, M. C. Jain, and M. H. Zarifi, "High-resolution, sensitivity-enhanced active resonator sensor using substrate-embedded channel for characterizing low-concentration liquid mixtures," *IEEE Trans. Microw. Theory Techn.*, vol. 70, no. 1, pp. 576–586, Jan. 2022.

[7] C.-H. Tseng, C.-H. Pai, and H.-C. Chang, "A new microwave oscillator-based microfluidic dielectric sensor," *IEEE Trans. Microw. Theory Techn.*, vol. 72, no. 1, pp. 628–637, Jan. 2024.

[8] J. Huang et al., "Oscillation-based active sensor on SIW reentrant cavity resonator for self-sustained ultralow concentration detection to saline solution," *IEEE Trans. Microw. Theory Techn.*, vol. 72, no. 9, pp. 5406–5419, Sep. 2024.

[9] A. A. Helmy et al., "A self-sustained CMOS microwave chemical sensor using a frequency synthesizer," *IEEE J. Solid-State Circuits*, vol. 47, no. 10, pp. 2467–2483, Oct. 2012.

[10] M. Pontón, S. Sancho, A. Herrera, and A. Suárez, "Oscillators based on step-impedance and slow wave transmission lines for sensing applications," *IEEE Trans. Microw. Theory Techn.*, vol. 71, no. 1, pp. 203–217, Jan. 2023.

[11] V. Lammert et al., "A K-band complex permittivity sensor for biomedical applications in 130-nm SiGe BiCMOS," *IEEE Trans. Circuits Syst. II, Exp. Briefs*, vol. 66, no. 10, pp. 1628–1632, Oct. 2019.

[12] F. I. Jamal, S. Guha, M. H. Eissa, D. Kissinger, and J. Wessel, "A low-power 30 GHz complex dielectric chem-bio-sensor in a SiGe BiCMOS technology," in *IEEE MTT-S Int. Microw. Symp. Dig.*, Gothenburg, Sweden, May 2017, pp. 1–4.

[13] B.-H. Kim et al., "A proximity coupling RF sensor for wrist pulse detection based on injection-locked PLL," *IEEE Trans. Microw. Theory Techn.*, vol. 64, no. 5, pp. 1667–1676, May 2016.

[14] S. Chen, M. Guo, K. Xu, P. Zhao, L. Dong, and G. Wang, "A frequency synthesizer based microwave permittivity sensor using CMRC structure," *IEEE Access*, vol. 6, pp. 8556–8563, 2018.

[15] F. I. Jamal et al., "Low-power miniature *K*-band sensors for dielectric characterization of biomaterials," *IEEE Trans. Microw. Theory Techn.*, vol. 65, no. 3, pp. 1012–1023, Mar. 2017.

[16] J.-C. Chien, E.-C. Yeh, L. P. Lee, M. Anwar, and A. M. Niknejad, "A microwave reconfigurable dielectric-based glucose sensor with 20 mg/dL sensitivity at sub-nL sensing volume in CMOS," in *IEEE MTT-S Int. Microw. Symp. Dig.*, Phoenix, AZ, USA, May 2015, pp. 1–4.

[17] M. Babay et al., "Highly sensitive capacitive sensor based on injection locked oscillators with ppm sensing resolution," in *IEEE MTT-S Int. Microw. Symp. Dig.*, Los Angeles, CA, USA, Aug. 2020, pp. 456–459.

[18] M. Pontón, S. Hernández, and A. Suárez, "Phase-sensitivity analysis of injection-locked mutually coupled oscillators," in *Proc. 47th Eur. Microw. Conf. (EuMC)*, Nuremberg, Germany, Oct. 2017, pp. 771–774, doi: 10.23919/EuMC.2017.8230961.

[19] J. Juillard, P. Prache, and N. Barniol, "Analysis of mutually injection-locked oscillators for differential resonant sensing," *IEEE Trans. Circuits Syst. I, Reg. Papers*, vol. 63, no. 7, pp. 1055–1066, Jul. 2016, doi: 10.1109/TCSI.2016.2553298.

[20] R. Mirzavand, M. M. Honari, and P. Mousavi, "High-resolution dielectric sensor based on injection-locked oscillators," *IEEE Sensors J.*, vol. 18, no. 1, pp. 141–148, Jan. 2018.

[21] J. Huang and Y. Xiang, "Injection-locked-oscillation-based active sensor on dual-mode folded SIW rectangular cavity for high-resolution detection to moisture and Fe particle in lubricant oil," *IEEE Trans. Microw. Theory Techn.*, vol. 71, no. 4, pp. 1600–1611, Apr. 2023.

[22] M. Pontón, A. Suarez, and S. Sancho, "Analysis of the nonlinear dynamics of an injection-locked dual-mode oscillator," *IEEE Trans. Microw. Theory Techn.*, vol. 72, no. 9, pp. 5120–5133, Sep. 2024.

[23] K. Huang and M. Hossein-Zadeh, "Detection and sensing using coupled oscillatory systems at the synchronization edge," *IEEE Sensors J.*, vol. 20, no. 21, pp. 12992–12998, Nov. 2020.

[24] M. Pontón, S. Sancho, and A. Suárez, "Analysis of a beat-frequency sensor operating near the locking boundary," *IEEE Trans. Microw. Theory Techn.*, early access, Apr. 2, 2025, doi: 10.1109/TMTT.2025.3552963.

[25] M. Abdolrazzaghi and M. Daneshmand, "Exploiting sensitivity enhancement in micro-wave planar sensors using intermodulation products with phase noise analysis," *IEEE Trans. Circuits Syst. I, Reg. Papers*, vol. 67, no. 12, pp. 4382–4395, Dec. 2020.

[26] A. Suárez, M. Pontón, and S. Sancho, "Analysis and design of material sensors based on free-running and injection-locked oscillators," in *IEEE MTT-S Int. Microw. Symp. Dig.*, San Juan, PR, USA, Jan. 2025, pp. 24–27.

[27] J. Jugo, J. Portilla, A. Anakabe, A. Suarez, and J. M. Collantes, "Closed-loop stability analysis of microwave amplifiers," *Electron. Lett.*, vol. 37, no. 4, pp. 226–228, Feb. 2001.

[28] N. Ayllon, J.-M. Collantes, A. Anakabe, I. Lizarraga, G. Soubercaze-Pun, and S. Forestier, "Systematic approach to the stabilization of multitransistor circuits," *IEEE Trans. Microw. Theory Techn.*, vol. 59, no. 8, pp. 2073–2082, Aug. 2011.
[29] E. Ngoya and R. Larcheveque, "Envelop transient analysis: A new method for the transient and steady state analysis of microwave communication circuits and systems," in *IEEE MTT-S Int. Microw. Symp. Dig.*, vol. 3, Jun. 1996, pp. 1365–1368, doi: 10.1109/MWSYM.1996.512189.
[30] T. Hastie, R. Tibshirani, J. H. Friedman, and J. H. Friedman, *The Elements of Statistical Learning: Data Mining, Inference, and Prediction*, 2nd ed., Cham, Switzerland: Springer, 2009.
[31] F. Ramírez, S. Sancho, and A. Suárez, "Oscillation modes in multiresonant oscillator circuits," *IEEE Trans. Microw. Theory Techn.*, vol. 64, no. 12, pp. 4660–4675, Dec. 2016.
[32] V. Rizzoli, A. Neri, and F. Mastri, "A modulation-oriented piecewise harmonic-balance technique suitable for transient analysis and digitally modulated signals," in *Proc. 26th Eur. Microw. Conf.*, Prague, Czech Republic, Oct. 1996, pp. 546–550, doi: 10.1109/euma.1996.337640.
[33] E. Ngoya, J. Rousset, and D. Argollo, "Rigorous RF and microwave oscillator phase noise calculation by envelope transient technique," in *IEEE MTT-S Int. Microw. Symp. Dig.*, vol. 1, Jun. 2000, pp. 91–94, doi: 10.1109/MWSYM.2000.860892.
[34] J. Roychowdhury, "Efficient methods for simulating highly nonlinear multi-rate circuits," in *Proc. 34th Annu. Conf. Design Autom. Conf.*, 1997, pp. 269–274, doi: 10.1145/266021.266092.
[35] H. G. Brachtendorf, G. Welsch, and R. Laur, "A time-frequency algorithm for the simulation of the initial transient response of oscillators," in *Proc. EEE Int. Symp. Circuits Syst.*, vol. 6, Feb. pp. 236–238, doi: 10.1109/ISCAS.1998.705255.
[36] J. C. Pedro and N. B. Carvalho, "Simulation of RF circuits driven by modulated signals without bandwidth constraints," in *IEEE MTT-S Int. Microw. Symp. Dig.*, vol. 3, Jun. 2002, pp. 2173–2176, doi: 10.1109/MWSYM.2002.1012302.
[37] L. D. Landau and E. M. Lifshitz, *Electrodynamics of Continuous Media*. New York, NY, USA: Pergamon Press, 1984.
[38] A. Sihvola, *Electromagnetic Mixing Formulas and Applications*. London, U.K.: IET, 1999.
[39] D. B. Leeson, "A simple model of feedback oscillator noise spectrum," *Proc. IEEE*, vol. 54, no. 2, pp. 329–330, Feb. 1966.
[40] C. Jany, A. Siligaris, J. L. Gonzalez-Jimenez, P. Vincent, and P. Ferrari, "A programmable frequency multiplier-by-29 architecture for millimeter wave applications," *IEEE J. Solid-State Circuits*, vol. 50, no. 7, pp. 1669–1679, Jul. 2015.
[41] V. Rizzoli, F. Mastri, and D. Masotti, "General noise analysis of nonlinear microwave circuits by the piecewise harmonic-balance technique," *IEEE Trans. Microw. Theory Techn.*, vol. 42, no. 5, pp. 807–819, May 1994.
[42] F. X. Kaertner, "Analysis of white and f-noise in oscillators," *Int. J. Circuit Theory Appl.*, vol. 18, pp. 485–519, Jan. 1990.
[43] A. Demir, A. Mehrotra, and J. Roychowdhury, "Phase noise in oscillators: A unifying theory and numerical methods for characterization," *IEEE Trans. Circuits Syst. I: Fundam. Theory Appl.*, vol. 47, no. 5, pp. 655–674, May 2000.
[44] M. Gil, P. Vélez, F. Aznar-Ballesta, J. Muñoz-Enano, and F. Martín, "Differential sensor based on electroinductive wave transmission lines for dielectric constant measurements and defect detection," *IEEE Trans. Antennas Propag.*, vol. 68, no. 3, pp. 1876–1886, Mar. 2020.
[45] A. Ebrahimi, G. Beziuk, J. Scott, and K. Ghorbani, "Microwave differential frequency splitting sensor using magnetic-LC resonators," *Sensors*, vol. 20, no. 4, p. 1066, Feb. 2020.
[46] G. Govind, N. K. Tiwari, K. K. Agrawal, and M. J. Akhtar, "Microwave imaging of subsurface defects in dielectric structures using complementary split ring resonator," in *Proc. 3rd Int. Conf. Microw. Photon. (ICMAP)*, Dhanbad, India, Feb. 2018, pp. 1–2.
[47] A. K. Jha, A. Lamecki, R. Gómez-García, and M. Mrozowski, "Near field coupled wireless microwave sensor," in *Proc. 23rd Int. Microw. Radar Conf. (MIKON)*, Warsaw, Poland, Oct. 2020, pp. 260–262.
[48] J.-Z. Bao, M. L. Swicord, and C. C. Davis, "Microwave dielectric characterization of binary mixtures of water, methanol, and ethanol," *J. Chem. Phys.*, vol. 104, no. 12, pp. 4441–4450, Mar. 1996.
[49] M. Abdolrazzaghi and M. Daneshmand, "A phase-noise reduced microwave oscillator sensor with enhanced limit of detection using active filter," *IEEE Microw. Wireless Compon. Lett.*, vol. 28, no. 9, pp. 837–839, Sep. 2018.
[50] H. Sun et al., "An active and portable alcohol solution concentrations sensing system based on microwave rectifier circuit," *IEEE Sensors J.*, vol. 24, no. 24, pp. 41767–41776, Dec. 2024.
[51] Y. Wang, S. Fu, X. Han, H. Chen, Z. Xu, and F. Martín, "High-sensitivity integrated oscillator-based differential microfluidic sensor," *IEEE Trans. Microw. Theory Techn.*, early access, Apr. 18, 2025, doi: 10.1109/TMTT.2025.3558920.
[52] H.-C. Chang, C.-T.-M. Wu, and C.-H. Tseng, "A 24-GHz frequency-locked loop-based microwave microfluidic sensor for concentration detection," *IEEE J. Sel. Areas Sensors*, vol. 1, pp. 20–28, 2024.

Mabel Pontón (Member, IEEE) was born in Santander, Spain. She received the bachelor's degree in telecommunication engineering, the master's degree in information technologies and wireless communications systems, and the Ph.D. degree from the University of Cantabria, Santander, in 2004, 2008, and 2010, respectively.

In 2006, she joined the Communications Engineering Department, University of Cantabria. From 2011 to 2013, she was with the Group of Electronic Design and Applications, Georgia Institute of Technology, Atlanta, GA, USA, as a Post-Doctoral Research Fellow. Her current research interests include nonlinear analysis and simulation of radio frequency and microwave circuits, with an emphasis on phase noise, stability, and bifurcation analysis of complex oscillator topologies.

Sergio Sancho (Senior Member, IEEE) received the Licentiate degree in electronic physics from Basque Country University, Leioa, Spain, in 1997, and the Ph.D. degree in electronic engineering from the Communications Engineering Department, University of Cantabria, Santander, Spain, in February 2002.

In 1998, he joined the Communications Engineering Department, University of Cantabria, where he currently works as an Associate Professor. His research interests include nonlinear analysis of microwave autonomous circuits and frequency synthesizers, including stochastic and phase-noise analysis.

Almudena Suárez (Fellow, IEEE) was born in Santander, Spain. She received the Licentiate degree in electronic physics and the Ph.D. degree from the University of Cantabria, Santander, Spain, in 1987 and 1992, respectively, and the Ph.D. degree in electronics from the University of Limoges, Limoges, France, in 1993.

She was an Invited Visiting Professor at California Institute of Technology (Caltech), Pasadena, CA, USA, from 2004 to 2005. She is currently a Full Professor with the University of Cantabria and the Head of the Research Group Microwave Engineering and Radiocommunication Systems. She has authored the book *Analysis and Design of Autonomous Microwave Circuits* (IEEE-Wiley, 2009) and co-authored the book *Stability Analysis of Nonlinear Microwave Circuits* (Artech House, 2003).

Prof. Suárez served as a Member of the Board of Directors of European Microwave Association from 2012 to 2020. In 2021, she received the Research Award from the Social Council of Universidad de Cantabria. In 2025, she received the IEEE MTT-S Distinguished Educator Award. She was also an IEEE Distinguished Microwave a Lecturer from 2006 to 2008. In addition, she served as the Coordinator of the Communications and Electronic Technology Area for Spanish National Evaluation and Foresight Agency from 2009 to 2013. She was the Chair of the 2014 and 2015 editions of IEEE Topical Conference on RF/Microwave Power Amplifiers (PAWR) in Newport Beach, CA, USA, and San Diego, CA. She was the General TPC Chair of European Microwave Week 2018. She was the General TPC Chair of the European Microwave Week (EuMW) in 2018. She was the Editor-in-Chief of *International Journal of Microwave and Wireless Technologies* from Cambridge University Press journals from 2013 to 2018. She was the Editor-in-Chief of IJMWT from 2013 to 2018. Since 2023, she has been the Editor-in-Chief of IEEE T-MTT.